frontiers in Materials

ORIGINAL RESEARCH
published: 25 January 2022
doi: 10.3389/fmats.2022.825592

Mechanism of CO_2 Capacity Reduction of Flexible Metal-Organic Framework Caused by Water Adsorption

Satoshi Watanabe, Shotaro Hiraide*, Hayato Kunimitsu, Atsushi Fujiwara and Minoru T. Miyahara*

Department of Chemical Engineering, Kyoto University, Kyoto, Japan

OPEN ACCESS

Edited by:
Tian Tian,
Imperial College London,
United Kingdom

Reviewed by:
David Danaci,
Imperial College London,
United Kingdom
Ying Xiong,
Autonomous University of Madrid,
Spain
Libo Li,
Taiyuan University of Technology,
China

****Correspondence:***
Satoshi Watanabe
nabe@cheme.kyoto-u.ac.jp
Shotaro Hiraide
hiraide@cheme.kyoto-u.ac.jp

Specialty section:
This article was submitted to Colloidal Materials and Interfaces, a section of the journal Frontiers in Materials

Received: *30 November 2021*
Accepted: *10 January 2022*
Published: *25 January 2022*

Citation:
Watanabe S, Hiraide S, Kunimitsu H, Fujiwara A and Miyahara MT (2022) Mechanism of CO_2 Capacity Reduction of Flexible Metal-Organic Framework Caused by Water Adsorption. Front. Mater. 9:825592. doi: 10.3389/fmats.2022.825592

Elastic layer-structured metal-organic framework (MOF)-11 {ELM-11: [$Cu(BF_4)_2$ (4,4′-bipyridine)$_2$]}, which is a crystalline porous material, is a promising adsorbent for high-throughput and high-efficiency separation processes of CO_2 because of its peculiar adsorption characteristics originating from the flexibility of the crystal framework. However, the exposure of ELM-11 to water vapor has been reported to reduce its CO_2 capacity, which is problematic for processing feed gases that contain a certain concentration of water vapor. In this study, we investigated the stability of ELM-11 against water vapor exposure to reveal the mechanism of CO_2 capacity reduction. Our combined measurements of adsorption isotherms and X-ray diffraction patterns indicated that the CO_2 capacity reduction was caused by the partial formation of a crystalline subphase upon adsorption of water molecules and the subsequent formation of an amorphous phase to relax the crystalline grain boundaries. Because a higher supply rate of water molecules resulted in a larger amount of subphase formation, we concluded that the structural subphase was a metastable kinetically controlled structure, formed through the rate-dependent adsorption of water molecules. These results suggest that slowing the adsorption rate is an effective approach to suppress the formation of the subphase; therefore, we proposed the covering of ELM-11 surfaces with porous shells. We used ELM-12 {[$Cu(CF_3SO_3)_2$ (4,4′-bipyridine)$_2$]} as a shell material because of its robust stability against water adsorption and affinity with ELM-11. The ELM-12 shell decreased the adsorption rate of water molecules compared with that of bare ELM-11, resulting in the suppression of subphase formation and preventing CO_2 capacity reduction. Although further optimization of the shell thickness and coverage is required to keep the capacity completely unchanged, controlling the adsorption rate of water molecules is successfully demonstrated to be possible with shell formation, which is key for industrial applications of ELM-11.

Keywords: ELMs, water vapor, flexible MOFs, adsorption isotherm, adsorption rate, coreshell particles, synergistic effect, cooperative transition

1 INTRODUCTION

The separation and recovery of CO_2, which is a representative greenhouse gas, is one of the most critical technologies for addressing the global warming issue (Leung et al., 2014). Among various techniques, including absorption, membrane separation, and cryogenic distillation, physical adsorption in porous media is an attractive approach because of its applicability to a wide range of gas concentrations and energy- and cost-saving characteristics (Samanta et al., 2012; Elfving et al., 2017; Bui et al., 2018). To further improve separation, energy, and cost efficiency, much effort has been devoted to developing novel adsorbent materials with high CO_2 capacities and selectivities (D'Alessandro et al., 2010). Metal-organic frameworks (MOFs), which are porous crystalline solids composed of metal ions and organic ligands, are emerging adsorbent materials because of their regularity and controllability of pore structures as well as the large surface areas and pore volumes (Belmabkhout et al., 2016). Several high-performing MOFs for CO_2 separation have been strategically proposed with the aid of recent advances in screening and optimization techniques from a large number of combinations of metal ions and organic ligands (Avci et al., 2020; Burns et al., 2020).

Elastic layer-structured MOF-11 {ELM-11 [$Cu(BF_4)_2$ $(bpy)_2$]; bpy = 4,4′-bipyridine} is a promising candidate MOF with a stacking structure of two-dimensional (2D) square grid sheets composed of Cu ions, bpy molecules, and BF_4 anions binding to Cu ions in a direction perpendicular to a 2D layer (Li and Kaneko, 2001; Kanoh et al., 2009). ELM-11 exhibits flexibility in the stacking structure to expand interspaces between 2D layers so that guest molecules are suddenly adsorbed at a threshold pressure, at which ELM-11 opens the "gates" by expanding the interlayer distances (Kondo et al., 2006; Hiraide et al., 2016). This results in stepped adsorption isotherms, which are so-called gate adsorption isotherms. An adsorbent material with stepped isotherms is suitable for pressure and/or temperature swing adsorption (P/TSA) processes, in which adsorption and desorption cycles are operated by swinging the pressure and/or temperature, because a high working capacity, which is defined by the difference between the adsorbed amounts in adsorption and desorption processes, is possible with a narrow range of pressure and temperature swing in P/TSA processes (Mason et al., 2015; McDonald et al., 2015). In fact, ELM-11 has been demonstrated to enable high-throughput separation of CO_2 from a CO_2/CH_4 gas mixture in a model system of the PSA (Hiraide et al., 2020). This was possible by taking advantage of the stepped isotherms in combination with the fast kinetics of the gating and intrinsically endothermic nature of the framework expansion to compensate for the heat of adsorption. In addition, ELM-11 has been demonstrated to be a robust framework after 100 consecutive runs of adsorption and desorption of *n*-butane and nitrogen without noticeable changes in its adsorption properties (Bon et al., 2015), which is quite suitable for P/TSA processes.

A key requirement for adsorbent materials is their tolerance to water exposure, as water is usually present in feed gases in a variety of concentrations. Cheng et al. reported that ELM-11 maintained a saturated adsorbed amount of CO_2 by a regeneration procedure after water vapor adsorption (Cheng et al., 2009). However, the shape of the stepped isotherms of CO_2 after water adsorption became less steep and the particle morphology became less defined with smaller sizes, which clearly indicated the impact of water exposure on ELM-11. Furthermore, Sotomayor and Lastoskie recently reported that repeated exposure of ELM-11 to water vapor degraded its CO_2 capacity (Sotomayor and Lastoskie, 2020), suggesting that the effects of water exposure accumulate during the adsorption and desorption cycles of water molecules. This is a significant problem because the adsorption and desorption cycles are repeated in the PSA and TSA processes. To apply ELM-11 practically in CO_2 separation and recovery, it is necessary to determine the cause of the CO_2 capacity reduction against water exposure and to develop a detailed understanding of the roles of water adsorption and desorption for a possible solution to the problem.

In this study, we investigated the effects of water adsorption on the crystalline structure, adsorption behavior, and thermal stability of ELM-11. We employed two procedures for water adsorption in ELM-11, which involved the use of an automated adsorption apparatus and direct exposure to the atmosphere, to clarify the mechanism of the CO_2 capacity reduction against water exposure. Furthermore, based on the results obtained, we proposed a possible solution to suppress the CO_2 capacity reduction by encapsulating ELM-11 particles in the shell domains. We selected ELM-12 {[Cu $(CF_3SO_3)_2$ $(bpy)_2$]} (Kondo et al., 2007; Li et al., 2017; Li et al., 2018), which is a structural analog of ELM-11, as the shell material to synthesize ELM-11@ELM-12 core-shell particles and evaluated the effects of shell formation on the variations in crystalline structures and adsorption behaviors against water exposure.

2 EXPERIMENTAL

2.1 Materials

Copper (II) tetrafluoroborate [$Cu(BF_4)_2$, 45% aqueous solution] and copper (II) trifluoromethanesulfonate [$Cu(CF_3SO_3)_2$, 98%] were purchased from Alfa Aesar, Thermo Fisher Scientific Inc. and Sigma-Aldrich Co. LLC. (United States), respectively. 4,4′-bipyridyl (bpy, 98.0%) and nitric acid (67%) were purchased from Tokyo Chemical Industry Co., Ltd. (Tokyo, Japan). Methanol (99.8%) and ethanol (99.5%) were purchased from Kishida Chemical Co., Ltd. (Japan). All chemicals were used as received. Solutions with the desired concentrations were prepared by dissolving the original chemicals in ultrapure water (>18 MΩ cm, Arium mini, Sartorius, Germany). As a reference, pre-ELM-11 ({[Cu(bpy) $(BF_4)_2(H_2O)_2$](bpy)}, where the prefix "pre" refers to the hydrated form of ELM-11) powder was purchased from Tokyo Chemical Industry Co., Ltd.

2.2 Synthesis of ELM-11 Particles

Bpy methanol solution (1.5 ml) was added dropwise into a $Cu(BF_4)_2$ aqueous solution (1.5 ml) in a vial under stirring at 1,500 rpm using a magnetic stirrer. The dropwise addition was completed in ca. 3 min, followed by mixing at 1,500 rpm for 1 day. The reaction solution quickly turned turbid upon droplet

addition, indicating the formation of pre-ELM-11 particles. Notably, the as-synthesized particles are assumed to be pre-ELM-11 because of the inclusion of solvent water molecules (Blake et al., 1997) and the removal of water molecules transforms pre-ELM-11 into ELM-11 (Kondo et al., 2006). The synthesized particles were collected by vacuum filtration, washed with ultrapure water, and dried under vacuum overnight. The typical concentration conditions were $[Cu(BF_4)_2]$ = 200 mM and [bpy] = 400 mM, which is referred to as "synthesis-I." A higher concentration set was also used, $[Cu(BF_4)_2]$ = 1.6 M and [bpy] = 3.2 M, which was referred to as "synthesis-II."

2.3 Synthesis of ELM-12 Particles

10 ml of a bpy ethanol solution (80 mM) was added to 10 ml of a $Cu(CF_3SO_3)_2$ aqueous solution (40 mM) set in a vial. The reaction solution turned turbid within a few seconds, indicating the formation of ELM-12 particles, and was stirred at 1,500 rpm on a magnetic stirrer for 15 min. The resultant particles were collected by vacuum filtration, washed with ethanol, and dried under vacuum overnight.

2.4 Synthesis of ELM-11@ELM-12 Core-Shell Particles

Pre-ELM-11 particles synthesized in 2.2 were dispersed in ethanol and sonicated for 30 min, and then a bpy ethanol solution was added to prepare a mixed suspension of 40 mg/ml of pre-ELM-11 and 80 mM of bpy. 1.5 ml of a $Cu(CF_3SO_3)_2$ aqueous solution (40 mM) was added dropwise for ca. 3 min into 1.5 ml of the mixed suspension set in a vial under stirring at 1,500 rpm. Subsequently, the stirring was stopped and the reaction suspension was maintained still for 15 min. The resultant particles were collected by vacuum filtration, washed with ethanol, and dried under vacuum overnight.

2.5 Water Vapor Adsorption in ELM Particles

To introduce water molecules into the ELM particles, we applied two different procedures: the use of an automated apparatus for adsorption isotherm measurements and exposure to the atmosphere. Before each operation of the water vapor adsorption, the ELM particles were activated by degassing at 373 K for 12 h under vacuum below 10 Pa. The adsorption isotherm measurements of water vapor in the ELM particles were conducted at 303 K using an automated adsorption apparatus (BELSORP-max, MicrotracBEL Corp., Japan), in which the equilibrium setting was pressure variation of 0.3% for 600 s and the sample amount was approximately 25 mg. After reaching a saturated adsorption amount of water molecules, the ELM particles were removed from the sample cell and then used for powder X-ray diffraction (XRD) and CO_2 adsorption isotherm measurements. In the exposure process to the atmosphere, the ELM particles activated by the above procedure were spread on a glass slide and exposed to air with a humidity of ca. 30% at room temperature (ca. 20°C) for 5 min, and then analyzed by XRD, thermogravimetric analysis (TGA), and CO_2 adsorption isotherm measurements. Before each isotherm measurement of CO_2, the ELM particles after the water adsorption processes were activated by the procedure described above.

2.6 Characterization

Powder XRD patterns were recorded using an X-ray diffractometer, UltimaIV/285/DX (Rigaku Corp., Japan) with Cu Kα radiation (40 kV and 40 mA) at a scan rate of 5.0°/min and step size of 0.05°. The time course of the *in situ* powder XRD patterns of as-synthesized pre-ELM-11 particles during the activation process at 373 K under vacuum was measured on the BL02B2 beamline of the SPring-8 synchrotron facility, Japan, using incident X-rays with a wavelength of 0.0799932 nm and a large Debye-Scherrer-type diffractometer with a multi-modular system constructed with six MYTHEN detectors (Kawaguchi et al., 2017). In the *in situ* XRD measurements, pre-ELM-11 particles were set in a glass capillary, and the temperature of the capillary was controlled by a nitrogen gas blower. Scanning electron microscopy (SEM) and elemental mapping images were obtained using a SU8220 field emission SEM (Hitachi High-Tech Corp., Japan) equipped with an energy-dispersive X-ray spectroscope (EDX, EMAX Evolution, Horiba, Japan). The average particle size was calculated by measuring the size of at least 50 particles from the SEM images. TGA was conducted using a DTG-60H thermogravimetric analyzer (Shimadzu Corp., Japan) under a nitrogen flow of 50 ml/min at a heating rate of 3°C/min up to 300°C. The mass ratio of ELM-11 to ELM-12 in ELM-11@ELM-12 particles was calculated based on the amounts of boron and sulfur atoms which were measured by using an ICPS-7500 inductively coupled plasma (ICP) instrument (Shimadzu Corp., Japan) after dissolving 10 mg of the synthesized particles in 6 ml of a nitric acid aqueous solution prior to analysis. The adsorption isotherms of CO_2 gas in the synthesized ELM particles at 273 K were measured using a BELSORP-mini (MicrotracBEL Corp., Japan), in which the equilibrium setting was pressure variation within 30 Pa for 600 s and the sample amount was approximately 25 mg. The adsorption rate of water vapor at 298 K was measured using a house-made apparatus, in which the pressure variation was traced when water vapor was supplied to a sample cell by opening a valve connected to a manifold filled with water vapor at 2.8 kPa. The sample amount was approximately 20 mg. Before each adsorption measurement, the ELM particles were activated by degassing at 373 K for 12 h under vacuum below 10 Pa for pre-ELM-11 and pre-ELM-11@ELM-12 and at 363 K for 2 h under vacuum below 10 Pa for ELM-12.

3 RESULTS AND DISCUSSION

3.1 CO_2 Capacity and Structural Variation of ELM-11 After Water Adsorption

Figure 1 displays the classification of ELM-11 samples with different treatment procedures and synthetic conditions, the corresponding XRD patterns, and the adsorption isotherms. The XRD pattern of the as-synthesized particles (**Figure 1B**-a)

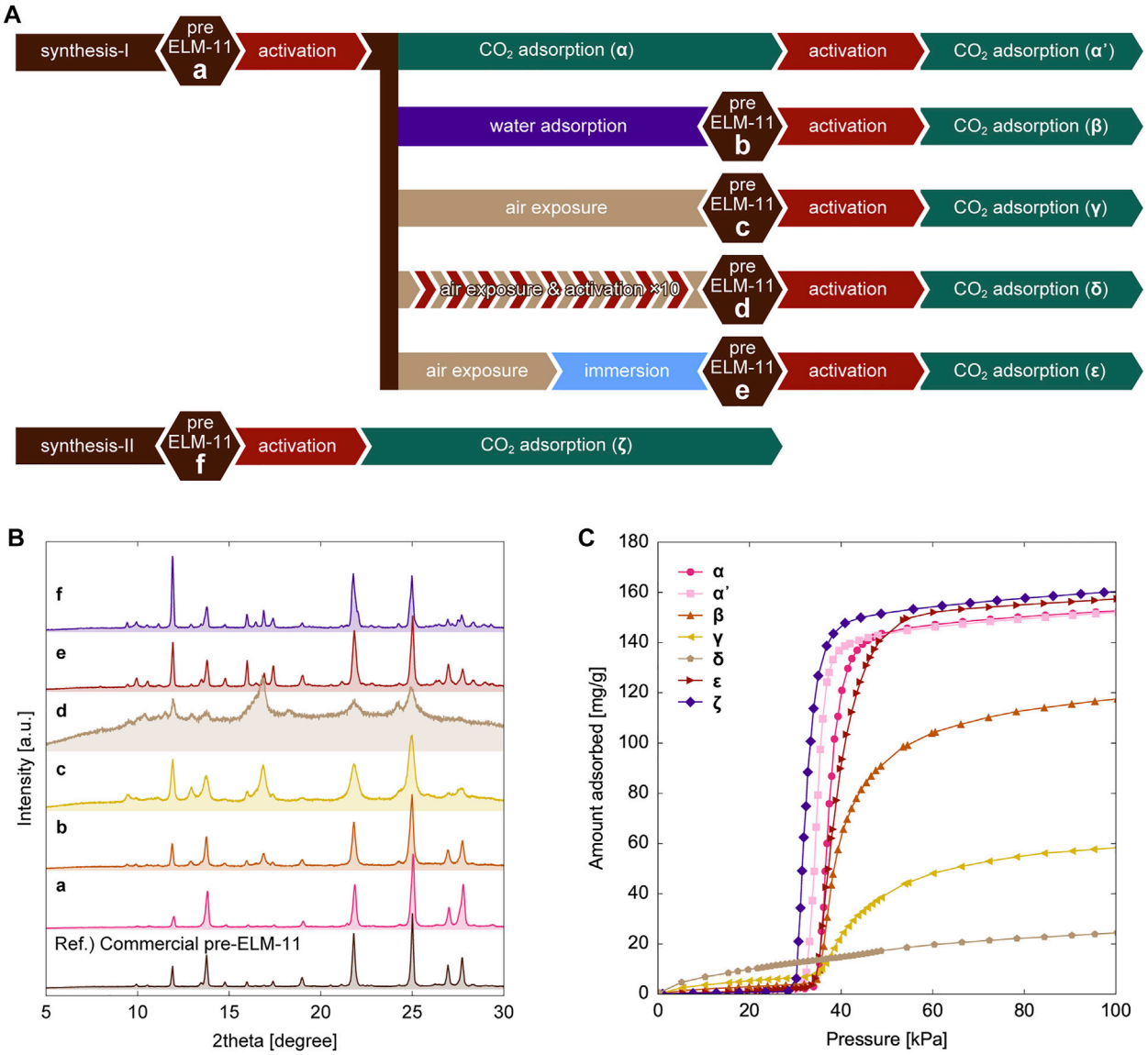

FIGURE 1 | (A) Classification of ELM-11 samples with different treatment procedures and synthetic conditions, **(B)** XRD patterns with labels from a to f which correspond to those in A and **(C)** adsorption isotherms of CO_2 at 273 K in samples with labels from α to ζ which correspond to those in A.

agreed fairly well with that of the commercial pre-ELM-11 particles, which were used as a reference, demonstrating the successful synthesis of pre-ELM-11 particles. Pre-ELM-11 transforms into ELM-11 by the removal of water molecules through the activation procedure at 373 K under vacuum (Kondo et al., 2006), and **Figure 1C**-*α* shows the adsorption isotherm of CO_2 gas in ELM-11 particles at 273 K. The adsorption amount sharply increased from almost zero to 140 mg/g at approximately 35 kPa, which was attributed to the gate adsorption caused by the structural transition from a closed nonporous structure to an open porous structure. After the adsorption and desorption measurements, we again activated the ELM-11 sample by degassing at 373 K under vacuum without exposure to air and conducted the second adsorption isotherm measurement (**Figure 1C**-*α*'). Although the gate adsorption started at a lower pressure than that in the first measurement, possibly because of stacking faults between 2D layers formed upon desorption of CO_2 molecules, the saturated adsorption capacity in the second measurement did not change significantly from that in the first measurement, demonstrating that no pore volume reduction resulted from the second CO_2 adsorption measurement. However, after the water vapor adsorption measurement (**Supplementary Figure S1**), the saturated adsorption amount of CO_2 decreased from 152 to 117 mg/g (**Figure 1C**-*β*), a trend similar to that previously reported (Sotomayor and Lastoskie, 2020). As shown in the XRD pattern of the ELM particles after water adsorption (**Figure 1B-b**), new peaks appeared at approximately 9°, 13°,

TABLE 1 | Crystallographic data for pre-ELM-11 and the subphase obtained from structural analysis.

Structure	Pre-ELM-11	Subphase
formula	$CuB_2C_{20}N_4H_{16}F_8{\cdot}2H_2O$	$CuB_2C_{20}N_4H_{16}F_8{\cdot}2H_2O$
space group	*C*2/*c* (No. 15)	*P*1 (No. 1)
a [nm]	1.6431	0.7451
b [nm]	1.1085	0.8180
c [nm]	1.4230	1.0069
α [°]	90	105.338
β [°]	115.407	99.512
γ [°]	90	107.711
V [nm^3]	2.3411	0.5856
Z	4	1

and 17° that were not observed in the XRD pattern of the as-synthesized particles (**Figure 1B**-a). Furthermore, the exposure of activated ELM-11 particles to the atmosphere decreased the saturated adsorption amount by 60% from 152 to 58 mg/g (**Figure 1C**-γ), and the intensity of the new peaks at around 9°, 13°, and 17° in the corresponding XRD pattern (**Figure 1B**-c) remarkably increased. In contrast, the water exposure gave little effects on desorption isotherms as shown in **Supplementary Figure S2**.

To identify the new peaks generated by water adsorption, we analyzed the XRD patterns using the indexing program CONOGRAPH (Esmaeili et al., 2017). As shown in **Table 1**, we found that the XRD pattern contained two phases: a monoclinic structure with cell parameters similar to those of pre-ELM-11 reported by Blake et al. (1997) and a triclinic structure. This result indicated that water adsorption not only transformed ELM-11 back into pre-ELM-11 but also induced the formation of a structural subphase. We then constructed a structural model of the subphase with reference to the pre-ELM-11 structure and relaxed the atomic arrangements of the structural model through density functional theory (DFT) calculations using the CP2K program (Hutter et al., 2014) (see **Supplementary Material** for more details). **Figure 2** shows the obtained subphase structure and its simulated XRD pattern together with those of pre-ELM-11, where the structural model of pre-ELM-11 was obtained from the structural relaxation for the reported structure whose cell parameters were adjusted to those tabulated in **Table 1** (crystallographic information files of the pre-ELM-11 and the subphase are available at https://github.com/2koza/CO2CapacityReduction). Although further refinement of the structural models by the Rietveld analysis was quite difficult to implement because the measured XRD pattern contained two phases, the simulated XRD patterns of the two structural models successfully accounted for all the peaks of the measured XRD pattern (**Figure 2A**), which confirms the validity of our structural model for the subphase. Based on our analyses, the major component was pre-ELM-11, which was composed of 2D layers with a zigzag alignment of square grids (**Figure 2B**), and the subphase was an isomer of pre-ELM-11 with a straight alignment of square grids in 2D layers (**Figure 2C**). According to the DFT calculations, pre-ELM-11 with the zigzag alignment was energetically more favored than the subphase with the straight alignment by 5.5 kJ/mol-Cu, which would be related to the fact that the closed structure of ELM-11 after the activation also has a zigzag alignment of square grids (Hiraide et al., 2016). Although both the water vapor adsorption measurement and the air exposure acted equally in terms of introducing water molecules into the ELM-11 framework, the difference between the two operations was the rate of supply of water. The adsorption measurement started from a low relative pressure of order 10^{-3} to gradually supply water molecules, while the air exposure instantaneously put ELM-11 particles at high relative pressure on the order of 10^{-1}. This indicates that the formation of the structural subphase is dependent on the water supply rate and, accordingly, a kinetically controlled phenomenon.

The formation of the structural subphase with peaks at around 9°, 13°, and 17° was detected not only in ELM-11 particles exposed

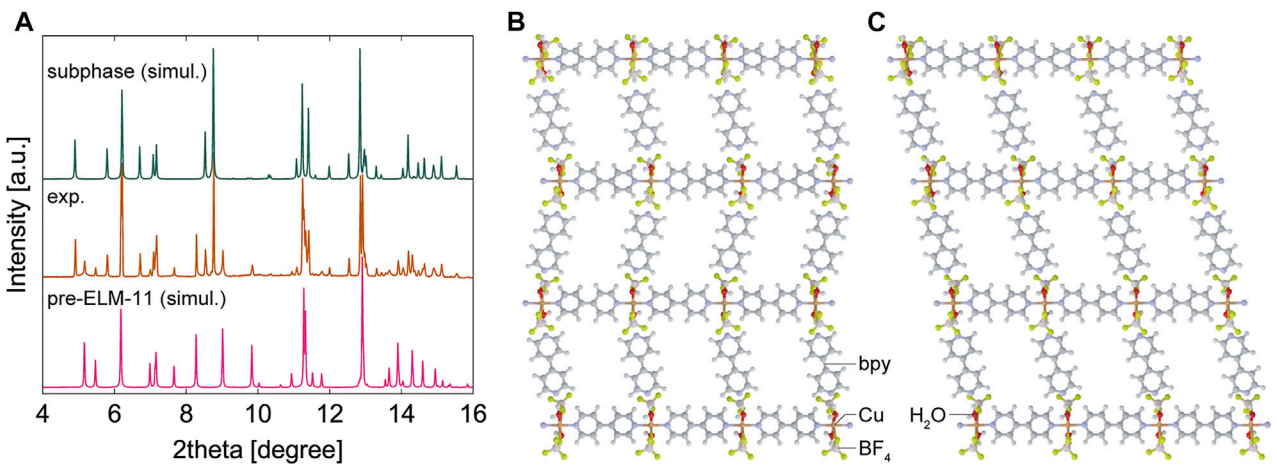

FIGURE 2 | Results of structural analyses. **(A)** Simulated XRD patterns of structural models for pre-ELM-11 and the isomeric subphase in comparison with a synchrotron XRD pattern of as-synthesized particles from "synthesis-II" condition that contained the two structural phases. We used the as-synthesized particles from "synthesis-II" condition instead of air-exposed samples because a stronger and sharper peak profile was obtained, which was suitable for detailed structural analyses. Top view of 2D layer of structural models for **(B)** pre-ELM-11 and **(C)** the isomeric subphase.

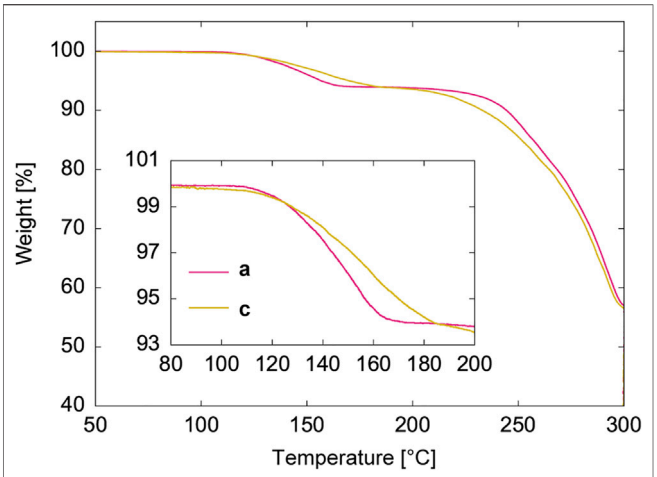

FIGURE 3 | TGA profiles of as-synthesized pre-ELM-11 particles (a) and air-exposed particles (c). The labels of a and c correspond to those in **Figure 1A**. Inset is a magnified graph in a temperature range from 80 to 200°C.

to water vapor (**Figure 1B**-b and **Figure 1B**-c) but also in the as-synthesized particles from the "synthesis-II" condition (a higher concentration set), as shown in **Figures 1B**-f. The subphase formation during the synthesis under a higher concentration condition would happen because some portions of the resultant particles were trapped in the metastable subphase, with less time for the structural rearrangement into the most stable pre-ELM-11 structure because of the higher reaction rate. However, we confirmed that the as-synthesized particles at a higher concentration transformed into ELM-11 during the activation process through *in situ* synchrotron XRD measurements (**Supplementary Figure S3**). Furthermore, their adsorption behavior was rather typical of ELM-11 with a saturated adsorption amount of CO_2 higher than 160 mg/g (**Figure 1C**-ζ), which demonstrated that the CO_2 capacity reduction observed in ELM-11 exposed to water vapor (**Figure 1C**-β and **Figure 1C**-γ) was not directly associated with the formation of the structural subphase.

Another noticeable feature in the XRD patterns after the water vapor exposure (**Figure 1B-b** and **Figure 1B-b**-c) was the increased amorphous phase indicated by the background (the shaded area in the XRD pattern). Therefore, the inclusion of water molecules not only transformed ELM-11 into crystal phases of pre-ELM-11 and its isomeric structural subphase but also produced an amorphous phase that possibly relaxed and stabilized structures at the crystalline domain boundaries. Because the background intensity increased in the following order: the as-synthesized (**Figure 1B**-a) < the water adsorption (**Figure 1B**-b) < the air exposure (**Figure 1B**-c), which correlated well with the order of the CO_2 capacity reduction (**Figure 1C**-α, β, γ), the formation of amorphous domains would be the cause of the CO_2 capacity reduction. To further confirm this trend, we treated the as-synthesized particles with 10 cycles of air exposure and activation processes (**Figure 1A**-d). This repeated air exposure resulted in a considerable decrease in the CO_2 capacity to 23 mg/g (**Figure 1C**-δ) accompanied by a significant increase in the amorphous nature (**Figure 1B**-d), thereby demonstrating a close relationship between the amorphous formation and the CO_2 capacity reduction.

Figure 3 shows the TGA profiles of the as-synthesized (**Figure 1A-a**) and air-exposed ELM particles (**Figures 1A-a**-c). The as-synthesized pre-ELM-11 particles from the synthesis-I condition exhibited a two-step weight loss starting at approximately 100°C. The weight loss in the first step from 100 to 170°C was measured to be 6%, which was attributed to the removal of water molecules in the pre-ELM-11 framework because the theoretical weight fraction of water molecules in pre-

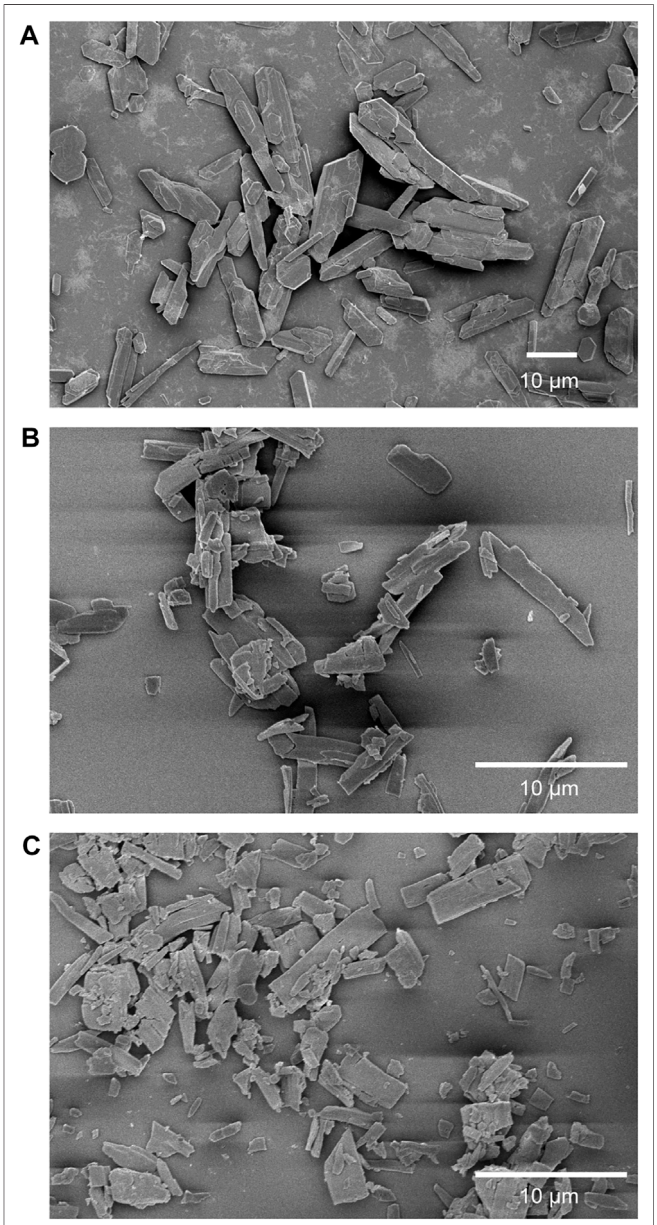

FIGURE 4 | SEM images of **(A)** as-synthesized pre-ELM-11 particles (a), **(B)** particles after the water adsorption measurement (b), and **(C)** particles after 10 cycles of air exposure and activation (d). The labels of a, b, and d correspond to those in **Figure 1A**.

ELM-11 was calculated to be 6.2% based on the stoichiometric ratio. The second step, at 200°C, is due to the thermal decomposition of the host framework. Meanwhile, the air-exposed particles showed a weight loss over a wider temperature range, from 50 to 190°C, when compared with the as-synthesized particles, indicating that the bonding states of water molecules introduced by the air exposure were less uniform than those in the as-synthesized pre-ELM-11 particles. This wider temperature range of weight loss is attributable to the existence of the amorphous phase. Because the weight loss of the air-exposed particles from 50 to 190°C was also 6%, this indicates that the water content was the same as that of the as-synthesized particles. However, given the amorphous nature of this air-exposed material, some water molecules were assumed to be trapped in different locations from those assigned to the pre-ELM-11 framework, and local domains with "wrong" locations of water molecules would be associated with the amorphous phase. Furthermore, the second step of the weight loss started at 190°C, a lower temperature than pre-ELM-11, indicating that the bpy molecules and BF_4 anions broke away from the amorphous phase, possibly because of the mislocation of water molecules.

The introduction of water molecules in ELM-11 also involved changes in particle size and shape. As shown in **Figure 4A**, the as-synthesized particles were rectangular-shaped with average long and short axes of 13.4 and 4.4 μm, respectively, while those after the water adsorption became smaller in size (average long and short axes of 5.6 and 1.3 μm, respectively), had less definition in shape, and some particles were fragmented into small pieces (**Figure 4B**). After the repeated air-exposure cycles, the particle size became much smaller (average long and short axes of 2.8 and 1.1 μm, respectively) and more fragments were present (**Figure 4C**). The broadening of the XRD peaks (**Figure 1B**-b, c, d) also demonstrated a decrease in the crystalline sizes caused by the water introduction procedures. The fragmentation of pre-ELM-11 particles was caused by the formation of a structural subphase upon water adsorption. Because the lattice constant is different between pre-ELM-11 and the subphase (**Table 1**), the coexistence of the two phases in the particles produces strains at the grain boundaries. The amorphous phase is then formed around the grain boundaries to relax the structural strains (Keblinski et al., 1997). When the strains produced in the particles are not relaxed by the formation of the amorphous phase enough to stabilize the grain boundaries, the particles are broken into smaller fragments.

We attempted to recrystallize the amorphous domains by immersing the air-exposed particles in the mother liquor of pre-ELM-11 particles, which was obtained as the supernatant of a pre-ELM-11 suspension after centrifugation, and stirred at 1,500 rpm for 1 day, followed by collection of particles by vacuum filtration and drying under vacuum overnight (**Figure 1A**-e). After this immersion procedure, the peak width was sharpened with a decreased background, as shown in **Figure 1B**-e. The recovery of the pre-ELM-11 structure in the sample after the immersion procedure was also supported by the adsorption isotherm measurement, as shown in **Figure 1C**-ε, because the saturated adsorption amount rebounded to that of the first measurement (**Figure 1C**-α). Therefore, a long-duration (1 day) immersion would have allowed constituent molecules in the amorphous phase to rearrange their locations to form the pre-ELM-11 framework.

Based on the results obtained so far, we propose a possible mechanism for the CO_2 capacity reduction of ELM-11 caused by water adsorption (**Figure 5**). The as-synthesized pre-ELM-11 transforms into ELM-11 by the activation process to remove water molecules, while the reintroduction of water molecules does not completely transform ELM-11 back into pre-ELM-11 but partially produces a structural subphase depending on the water supply rate. In the case of a slow supply rate of water molecules, such as water vapor adsorption measurements, water molecules are gradually introduced into ELM-11 frameworks so that they tend to find their proper locations to form coordination bonds with Cu ions in place of bpy molecules, which produces the most stable pre-ELM-11 as the main product. Meanwhile, a high supply rate due to air exposure, which instantaneously introduces water molecules into ELM-11, kinetically induces the formation of an isomer of pre-ELM-11 with a straight alignment of square grids. Because grain boundaries between the two crystalline phases produce strains in particles, amorphous structures are formed to relax and stabilize the boundary structures, and eventually, particles are fragmented at boundaries to release strains. Cycles of the activation and air exposure procedures further enhanced the formation of the subphase and amorphous structures. The removal of water molecules from the amorphous phase during the activation process does not produce ELM-11, possibly because of some missing bonds between Cu ions and bpy molecules, which naturally reduces the adsorption sites of CO_2 molecules. Thus, the CO_2 capacity reduction of ELM-11 is assumed to result primarily from a high supply rate of water molecules to induce the formation of metastable structural subphases and subsequent amorphous phases.

3.2 CO_2 Capacity Retention by ELM-12 Shell Formation

In the previous section, the supply rate of water to ELM-11 was demonstrated to be responsible for the CO_2 capacity of ELM-11. Based on the proposed mechanism, slowing the water supply rate is an effective approach for suppressing CO_2 capacity reduction. To achieve this, we propose the encapsulation of ELM-11 particles in porous shells with high stability against water adsorption. As a shell material, we selected ELM-12, which is a structural analog of ELM-11, firstly because ELM-12 demonstrated an almost constant CO_2 capacity against a cyclic exposure process of water vapor (Sotomayor and Lastoskie, 2020), and secondly because a seamless growth of the ELM-12 shell was expected on the ELM-11 particle surface due to the stacking layer structure of ELM-12 similar to that of pre-ELM-11 and ELM-11.

Figure 6 displays an XRD pattern of resultant particles synthesized by the procedure in **Section 2.4** along with those of pre-ELM-11 and ELM-12. All the diffraction peaks of the resultant particles were attributed to those of either pre-ELM-11 or ELM-12, demonstrating that the resultant particles were

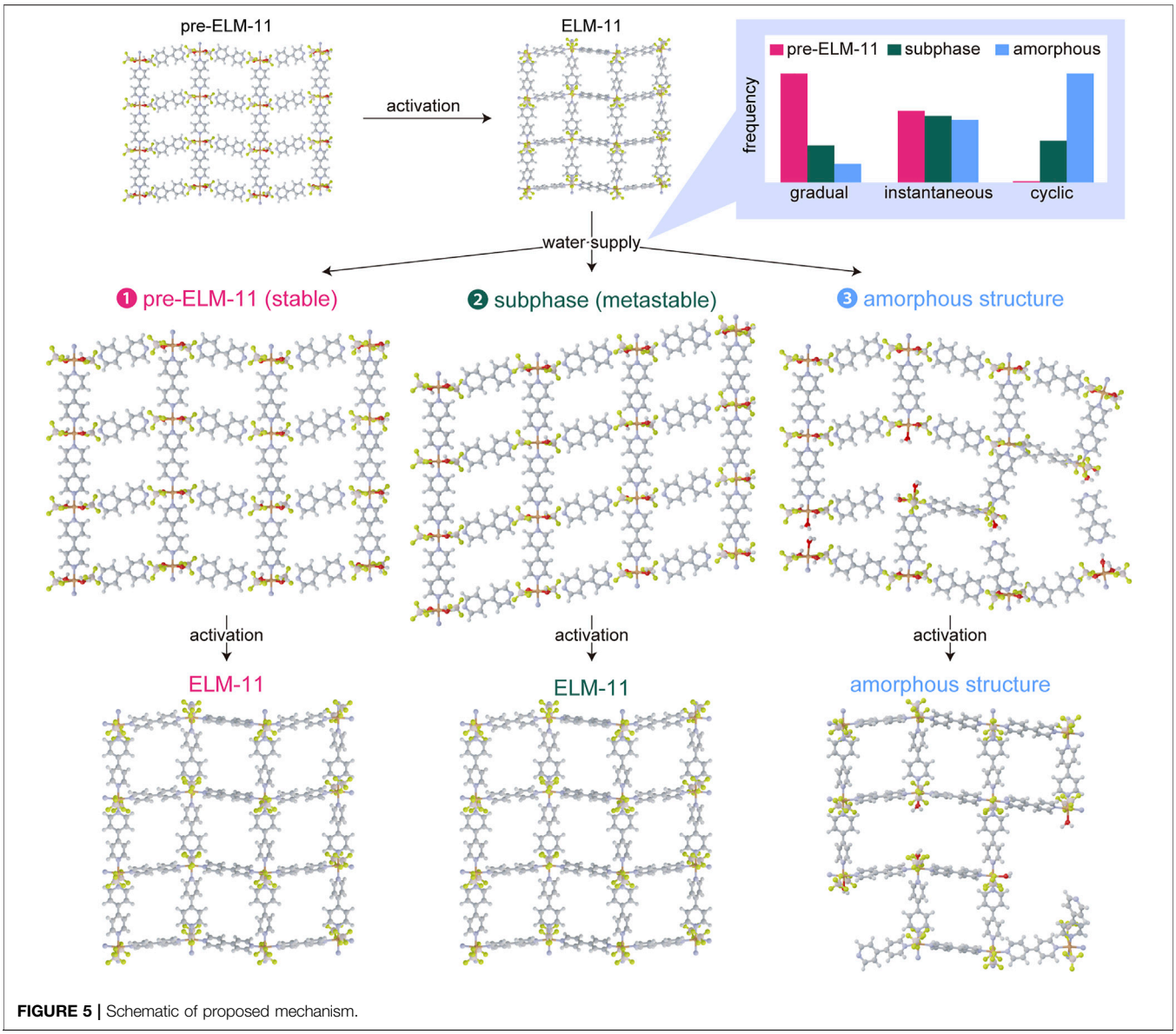

FIGURE 5 | Schematic of proposed mechanism.

composed of pre-ELM-11 and ELM-12. As shown in an SEM and the corresponding EDX mapping images of resultant particles in **Figure 7**, a fluorine domain in green was covered with sulfur domains in red. As references, we obtained separate EDX mapping images of pre-ELM-11 and ELM-12 particles and confirmed that only fluorine elements were detected in pre-ELM-11 particles, while sulfur elements were dominantly detected compared with fluorine elements in ELM-12 particles although ELM-12 contained both fluorine and sulfur elements (**Supplementary Figure S4**). These results demonstrated the formation of pre-ELM-11@ELM-12 core-shell-like particles, in which plate-like ELM-12 domains were deposited on rectangular-shaped pre-ELM-11 particles.

After the activation treatment of pre-ELM-11@ELM-12 particles at 373 K under vacuum, which was assumed to transform pre-ELM-11@ELM-12 into ELM-11@ELM-12, we

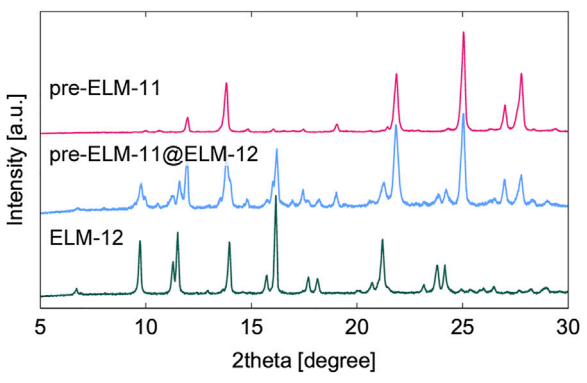

FIGURE 6 | XRD patterns of as-synthesized pre-ELM-11@ELM-12 particles in comparison with those of pre-ELM-11 and ELM-12 particles.

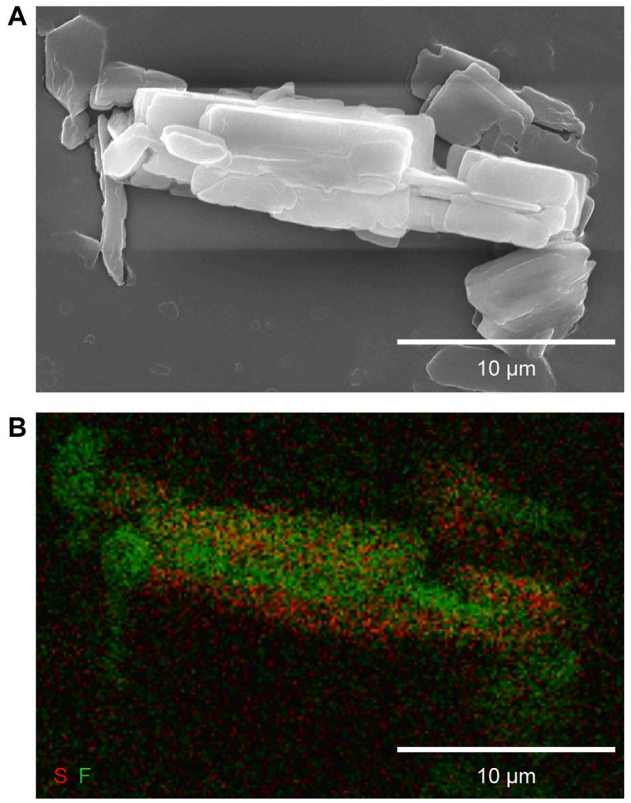

FIGURE 7 | (A) SEM and **(B)** EDX mapping images of as-synthesized pre-ELM-11@ELM-12 particles.

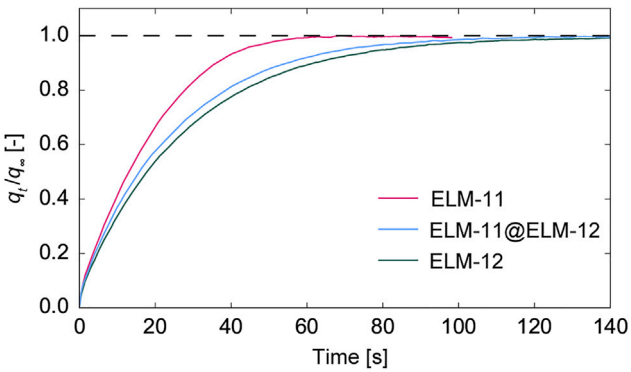

FIGURE 8 | Adsorption rates of water at 298 K in ELM-11, ELM-11@ELM-12, and ELM-12 particles.

measured the adsorption rate of water vapor in ELM-11@ELM-12 and compared it with those in ELM-11 and ELM-12. **Figure 8** shows the time course of q_t/q_∞, where q_t is the adsorption amount at time t, and q_∞ is that at equilibrium. The adsorption rate in ELM-11 was the fastest, whereas that of ELM-11@ELM-12 was the second but with a rate profile rather close to the slowest one of ELM-12, as confirmed by the time to reach, for example, q_t/q_∞ = 0.99, as 57, 106, and 136 s for ELM-11, ELM-11@ELM-12, and

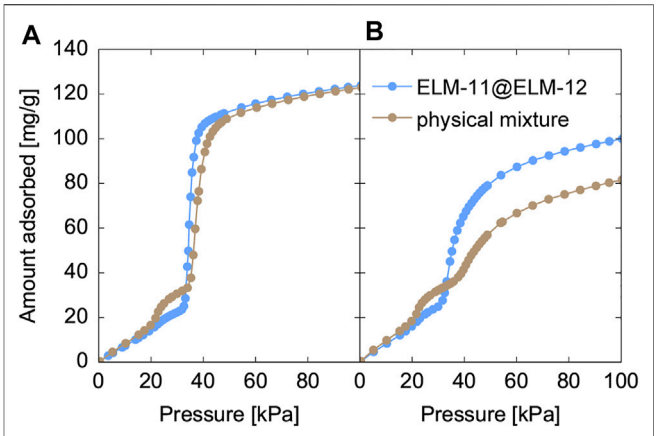

FIGURE 9 | Adsorption isotherms of CO_2 at 273 K in ELM-11@ELM-12 and a physical mixture of ELM-11 and ELM-12 **(A)** before and **(B)** after the air exposure.

ELM-12, respectively. These results clearly demonstrate that the formation of ELM-12 shells slowed the adsorption rate of water vapor.

Figure 9 shows the adsorption isotherms of CO_2 at 273 K in ELM-11@ELM-12 particles as well as a physical mixture of ELM-11 and ELM-12 particles (the desorption isotherms are shown in **Supplementary Figure S5**). The mixture ratio of ELM-11 to ELM-12 in the physical mixture was set to 1.8, which was the same as the composition ratio of ELM-11@ELM-12 particles measured by ICP analysis. The adsorption isotherm of ELM-11@ELM-12 gradually increased up to 35 kPa and exhibited subsequent steep uptake (**Figure 9A**). The initial gradual increase was attributed to the adsorption in ELM-12, while the steep uptake was attributed to the gate adsorption of ELM-11. A stepwise increase at 22 kPa, which was due to the gate adsorption in ELM-12, was suppressed in ELM-11@ELM-12 compared with that of the physical mixture. However, the saturated adsorption amount in ELM-11@ELM-12 was almost the same as that in the physical mixture, which indicated the simultaneous gate opening of ELM-11 and ELM-12 at 35 kPa through a cooperative structural transition in the core-shell structure, similar to the case of a zeolitic imidazolate framework-8 (ZIF-8)@ZIF-67 system (Fujiwara et al., 2021). Overall, the isotherm of ELM-11@ELM-12 was similar to that of the physical mixture except for the stepwise increase at 22 kPa, demonstrating that the CO_2 capacity and the gate adsorption characteristics of ELM-11 were kept unchanged against the encapsulation in the ELM-12 shell. However, after air exposure, the difference in the adsorption behavior was evident between the two samples (**Figure 9B**). The saturated adsorption amount in the physical mixture decreased by almost 35%, while the decrease in the CO_2 adsorption amount was suppressed in the ELM-11@ELM-12 particles. **Figure 10A** shows the XRD patterns of the ELM-11@ELM-12 particles and the physical mixture after air exposure. Although the difference in the background intensity was not evident between ELM-11@ELM-12 and the physical mixture, peaks specific to the pre-ELM-11 (not to the structural subphase), an example of which is

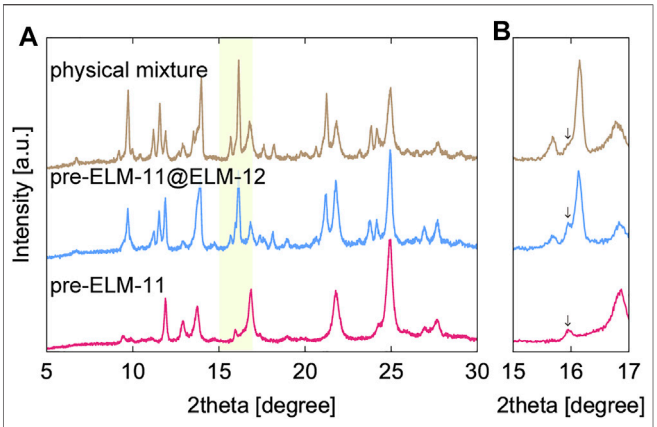

FIGURE 10 | (A) XRD patterns of ELM-11@ELM-12 and a physical mixture of ELM-11 and ELM-12 after the air exposure. As a reference, XRD pattern of ELM-11 after the air exposure is also shown, which is same as that in **Figure 1B**-c. **(B)** A magnified graph corresponding to the shaded area in A.

indicated by an arrow in **Figure 10B**, remained strong in ELM-11@ELM-12, while those in the physical mixture were weakened, indicating that the formation of the structural subphase was suppressed in ELM-11@ELM-12 particles. These results demonstrate that the ELM-12 shell slowed the supply rate of water vapor into ELM-11, which suppressed the subphase formation and subsequent formation of the amorphous phase. Although a complete inhibition of the CO_2 capacity reduction has not yet been achieved, which is possibly due to partial coverage of the ELM-11 surface, and further optimization would thus be needed on the shell coverage and thickness, the encapsulation of ELM-11 particles in ELM-12 shells was demonstrated to be a promising solution to the CO_2 capacity reduction of ELM-11 induced by water vapor adsorption.

4 CONCLUSION

We investigated the effects of water vapor exposure of ELM-11 on its crystalline structure, CO_2 capacity, and thermal stability. Our investigation demonstrated that the introduction of water molecules into the ELM-11 framework not only transformed its crystalline structure into pre-ELM-11 with a zigzag alignment of square grids but also induced the formation of a structural subphase, which turned out to be an isomer of pre-ELM-11 with a straight alignment of square grids. Isomer formation was assumed to induce the formation of an amorphous phase to relax and stabilize the crystalline grain boundaries, which caused the CO_2 capacity reduction of ELM-11 because the amorphous phase did not transform into ELM-11 upon the removal of water molecules. The comparison of the water adsorption procedure between the adsorption isotherm measurement and the direct exposure to the atmosphere suggested that the formation of the structural subphase was a kinetically controlled phenomenon that was dependent on the water supply rate to ELM-11. These results, in turn, suggest that slowing the water supply rate suppresses subphase formation. Accordingly, we proposed the encapsulation of ELM-11 particles in ELM-12 shells with high stability against water adsorption. The synthesis of ELM-12 shells successfully decreased the adsorption rate of water vapor compared with that of bare ELM-11, suppressed the formation of the subphase, and consequently prevented CO_2 capacity reduction to a certain extent. Although further optimization of the shell synthesis is needed to achieve complete suppression of the CO_2 capacity reduction, shell formation is a promising approach to control the adsorption kinetics of water vapor. The technique to synthesize core-shell MOFs not only reduces the weak properties of core MOFs but also enables the fabrication of porous materials with novel functionalities induced by synergistic effects between cores and shells, as observed in the cooperative structural transition between ELM-11 and ELM-12.

DATA AVAILABILITY STATEMENT

The original contributions presented in the study are included in the article/**Supplementary Material**, further inquiries can be directed to the corresponding authors.

AUTHOR CONTRIBUTIONS

SW designed the research project, acquired funding, supervised the project, and wrote the manuscript. SH conducted structural analyses and contributed with adsorption measurements, as one of the supervisors. HK conducted the experiments and wrote the manuscript. AF contributed with the synthesis of core-shell particles. MM contributed with instructions, as one of the supervisors.

FUNDING

This work was partly supported by the JSPS Grant-in-Aid for Scientific Research (B) (17H003443 and 21H01690), Fund for the Promotion of Joint International Research (Fostering Joint International Research (A), 18KK0411), and the Mukai Science and Technology Foundation.

ACKNOWLEDGMENTS

The authors are grateful to Y. Sakanaka, H. Arima, and R. Saitoh for their assistance with this work. The synchrotron radiation experiments were performed at the BL02B2 beamline of SPring-8 with the approval of the Japan Synchrotron Radiation Research Institute (JASRI) (proposal nos. 2020A1666, 2021A1588, 2021B1792, and 2021B1526).

SUPPLEMENTARY MATERIAL

The Supplementary Material for this article can be found online at: https://www.frontiersin.org/articles/10.3389/fmats.2022.825592/full#supplementary-material

REFERENCES

Avci, G., Erucar, I., and Keskin, S. (2020). Do New MOFs Perform Better for CO2 Capture and H2 Purification? Computational Screening of the Updated MOF Database. *ACS Appl. Mater. Inter.* 12, 41567–41579. doi:10.1021/acsami.0c12330

Belmabkhout, Y., Guillerm, V., and Eddaoudi, M. (2016). Low Concentration CO2 Capture Using Physical Adsorbents: Are Metal-Organic Frameworks Becoming the New Benchmark Materials? *Chem. Eng. J.* 296, 386–397. doi:10.1016/j.cej.2016.03.124

Blake, A. J., Hill, S. J., Hubberstey, P., and Li, W.-S. (1997). Rectangular Grid Two-Dimensional Sheets of Copper(II) Bridged by Both Co-Ordinated and Hydrogen Bonded 4,4′-bipyridine (4,4′-bipy) in [Cu(μ-4,4′-bipy)(H2O)2(FBF3) 2]·4,4′-bipy. *J. Chem. Soc. Dalton Trans.* 913, 913–914. doi:10.1039/A700036G

Bon, V., Kavoosi, N., Senkovska, I., and Kaskel, S. (2015). Tolerance of Flexible MOFs Toward Repeated Adsorption Stress. *ACS Appl. Mater. Inter.* 7, 22292–22300. doi:10.1021/acsami.5b05456

Bui, M., Adjiman, C. S., Bardow, A., Anthony, E. J., Boston, A., Brown, S., et al. (2018). Carbon Capture and Storage (CCS): The Way Forward. *Energy Environ. Sci.* 11, 1062–1176. doi:10.1039/c7ee02342a

Burns, T. D., Pai, K. N., Subraveti, S. G., Collins, S. P., Krykunov, M., Rajendran, A., et al. (2020). Prediction of MOF Performance in Vacuum Swing Adsorption Systems for Postcombustion CO2 Capture Based on Integrated Molecular Simulations, Process Optimizations, and Machine Learning Models. *Environ. Sci. Technol.* 54, 4536–4544. doi:10.1021/acs.est.9b07407

Cheng, Y., Kondo, A., Noguchi, H., Kajiro, H., Urita, K., Ohba, T., et al. (2009). Reversible Structural Change of Cu-MOF on Exposure to Water and its CO2 Adsorptivity. *Langmuir* 25, 4510–4513. doi:10.1021/la803818p

D'Alessandro, D. M., Smit, B., and Long, J. R. (2010). Carbon Dioxide Capture: Prospects for New Materials. *Angew. Chem. Int. Edition* 49, 6058–6082. doi:10.1002/anie.201000431

Elfving, J., Bajamundi, C., Kauppinen, J., and Sainio, T. (2017). Modelling of Equilibrium Working Capacity of PSA, TSA and TVSA Processes for CO 2 Adsorption under Direct Air Capture Conditions. *J. CO2 Utilization* 22, 270–277. doi:10.1016/j.jcou.2017.10.010

Esmaeili, A., Kamiyama, T., and Oishi-Tomiyasu, R. (2017). New Functions and Graphical User Interface Attached to Powder Indexing Software CONOGRAPH. *J. Appl. Cryst.* 50, 651–659. doi:10.1107/s1600576717001145

Fujiwara, A., Watanabe, S., and Miyahara, M. T. (2021). Flow Microreactor Synthesis of Zeolitic Imidazolate Framework (ZIF)@ZIF Core-Shell Metal-Organic Framework Particles and Their Adsorption Properties. *Langmuir* 37, 3858–3867. doi:10.1021/acs.langmuir.0c03378

Hiraide, S., Sakanaka, Y., Kajiro, H., Kawaguchi, S., Miyahara, M. T., and Tanaka, H. (2020). High-Throughput Gas Separation by Flexible Metal-Organic Frameworks with Fast Gating and Thermal Management Capabilities. *Nat. Commun.* 11, 3867. doi:10.1038/s41467-020-17625-3

Hiraide, S., Tanaka, H., and Miyahara, M. T. (2016). Understanding Gate Adsorption Behaviour of CO2 on Elastic Layer-Structured Metal-Organic Framework-11. *Dalton Trans.* 45, 4193–4202. doi:10.1039/c5dt03476k

Hutter, J., Iannuzzi, M., Schiffmann, F., and VandeVondele, J. (2014). CP2K: Atomistic Simulations of Condensed Matter Systems. *Wires Comput. Mol. Sci.* 4, 15–25. doi:10.1002/wcms.1159

Kanoh, H., Kondo, A., Noguchi, H., Kajiro, H., Tohdoh, A., Hattori, Y., et al. (2009). Elastic Layer-Structured Metal Organic Frameworks (ELMs). *J. Colloid Interf. Sci.* 334, 1–7. doi:10.1016/j.jcis.2009.03.020

Kawaguchi, S., Takemoto, M., Osaka, K., Nishibori, E., Moriyoshi, C., Kubota, Y., et al. (2017). High-Throughput Powder Diffraction Measurement System Consisting of Multiple MYTHEN Detectors at Beamline BL02B2 of SPring-8. *Rev. Scientific Instr.* 88, 085111. doi:10.1063/1.4999454

Keblinski, P., Phillpot, S. R., Wolf, D., and Gleiter, H. (1997). Amorphous Structure of Grain Boundaries and Grain Junctions in Nanocrystalline Silicon by Molecular-Dynamics Simulation. *Acta Materialia* 45, 987–998. doi:10.1016/S1359-6454(96)00236-4

Kondo, A., Noguchi, H., Carlucci, L., Proserpio, D. M., Ciani, G., Kajiro, H., et al. (2007). Double−Step Gas Sorption of a Two−Dimensional Metal−Organic Framework. *J. Am. Chem. Soc.* 129, 12362–12363. doi:10.1021/ja073568h

Kondo, A., Noguchi, H., Ohnishi, S., Kajiro, H., Tohdoh, A., Hattori, Y., et al. (2006). Novel Expansion/Shrinkage Modulation of 2D Layered MOF Triggered by Clathrate Formation with CO2 Molecules. *Nano Lett.* 6, 2581–2584. doi:10.1021/nl062032b

Leung, D. Y. C., Caramanna, G., and Maroto-Valer, M. M. (2014). An Overview of Current Status of Carbon Dioxide Capture and Storage Technologies. *Renew. Sustain. Energ. Rev.* 39, 426–443. doi:10.1016/j.rser.2014.07.093

Li, D., and Kaneko, K. (2001). Hydrogen Bond-Regulated Microporous Nature of Copper Complex-Assembled Microcrystals. *Chem. Phys. Lett.* 335, 50–56. doi:10.1016/S0009-2614(00)01419-6

Li, L., Lin, R.-B., Krishna, R., Wang, X., Li, B., Wu, H., et al. (2017). Flexible-Robust Metal-Organic Framework for Efficient Removal of Propyne from Propylene. *J. Am. Chem. Soc.* 139, 7733–7736. doi:10.1021/jacs.7b04268

Li, L., Lin, R.-B., Wang, X., Zhou, W., Jia, L., Li, J., et al. (2018). Kinetic Separation of Propylene over Propane in a Microporous Metal-Organic Framework. *Chem. Eng. J.* 354, 977–982. doi:10.1016/j.cej.2018.08.108

Mason, J. A., Oktawiec, J., Taylor, M. K., Hudson, M. R., Rodriguez, J., Bachman, J. E., et al. (2015). Methane Storage in Flexible Metal-Organic Frameworks with Intrinsic Thermal Management. *Nature* 527, 357–361. doi:10.1038/nature15732

McDonald, T. M., Mason, J. A., Kong, X., Bloch, E. D., Gygi, D., Dani, A., et al. (2015). Cooperative Insertion of CO2 in Diamine-Appended Metal-Organic Frameworks. *Nature* 519, 303–308. doi:10.1038/nature14327

Samanta, A., Zhao, A., Shimizu, G. K. H., Sarkar, P., and Gupta, R. (2012). Post-Combustion CO2 Capture Using Solid Sorbents: A Review. *Ind. Eng. Chem. Res.* 51, 1438–1463. doi:10.1021/ie200686q

Sotomayor, F. J., and Lastoskie, C. M. (2020). Carbon Dioxide Capacity Retention on Elastic Layered Metal Organic Frameworks Subjected to Hydrothermal Cycling. *Microporous Mesoporous Mater.* 304, 110377. doi:10.1016/j.micromeso.2020.110377

Conflict of Interest: The authors declare that the research was conducted in the absence of any commercial or financial relationships that could be construed as a potential conflict of interest.